Convective Interaction with Boundary-Layer Dynamics in the Development of a Tropical Intraseasonal System

BIN WANG AND TIANMING LI

Department of Meteorology, School of Ocean and Earth Science and Technology, University of Hawaii, Honolulu, Hawaii

ABSTRACT

Tropical boundary-layer flows interact with the free tropospheric circulation and underlying sea surface temperature, playing a critical role in coupling collective effects of cumulus heating with equatorial dynamics. In this paper a unified theoretical framework is developed in which convective interaction with large-scale circulation includes three mechanisms: convection–wave convergence (CWC) feedback, evaporation–wind (EW) feedback, and convection–frictional convergence (CFC) feedback. We examine the dynamic instability resulting from the convective interaction with circulation, in particular the role of CFC feedback mechanism.

CFC feedback results in an unstable mode that has distinctive characteristics from those occurring from CWC feedback or EW feedback in the absence of mean flow. The instability generated by CFC feedback is of low frequency with a typical growth rate on an order of 10^{-6} s^{-1}. The unstable mode is a multiscale wave packet; a global-scale circulation couples with a large-scale (several thousand kilometers) convective complex. The complex is organized by boundary-layer convergence and may consist of a few synoptic-scale precipitation cells. The heating released in the complex in turn couples the moist Kelvin wave and the Rossby wave with the gravest meridional structure, forming a dispersive system. The energy propagates slower than the individual cells within the wave packet. A transient boundary layer is shown to favor planetary-scale instability due to the frictionally created phase shift between the maximum vertical motion and the heating associated with boundary-layer convergence.

The implications of the theory to the basic dynamics of tropical intraseasonal oscillation are discussed.

1. Introduction

Madden and Julian's (1972) pioneering work suggested that the 40–50 day oscillation in the tropics is a result of eastward movement of large-scale cells oriented in the tropospheric equatorial plane. The early investigators of the oscillation, however, were hindered by the sparsity of observations. In the last ten years, satellite observations [e.g., outgoing longwave radiation (OLR)] and improved general circulation model (GCM) products have made available additional information concerning the nature of the oscillation (e.g., Lorenc 1984; Weickmann et al. 1985; Krishnamurti et al. 1985; Lau and Chan 1985, 1986; Murakami and Nakazawa 1985; Knutson and Weickmann 1987). Numerical simulations with various versions of GCMs have confirmed that the model's counterpart of the oscillation is indeed associated with eastward-migratory planetary-scale circulation systems (Lau and Lau 1986; Hayashi and Sumi 1986; Hayashi and Golder 1986, 1988; Swinbank et al. 1988; Lau et al. 1988). Recent analyses of pentad-mean anomaly maps of OLR and

ECMWF (European Centre for Medium-Range Forecasts) tropospheric winds have made it possible to objectively identify *individual* low-frequency convection and circulation anomalies and to document their development, movement, and dynamic structure (Wang and Rui 1990a; Weickmann and Khalsa 1990; Rui and Wang 1990). These low-frequency anomalies will be called tropical intraseasonal systems (TIS). The characteristic frequency of TIS is on an order of 10^{-6} s^{-1}, which is in between synoptic-scale (10^{-5} s^{-1}) and annual (10^{-7} s^{-1}) variations.

A fundamental theoretical problem has been the explanation of the origin and evolution of TIS. It is believed that condensational heating associated with deep convection is a primary energy source for the development and maintenance of these long-lasting planetary-scale systems (Krishnamurti et al. 1985; Murakami and Nakazawa 1985; Wang 1988). Extratropical forcing or Rossby wave penetration from midlatitude to the tropics may possibly serve as triggering mechanisms (Murakami 1988; Hsu et al. 1990).

A key element of the theoretical modeling of TIS deals with the interaction between convective heating and large-scale circulation. Various hypotheses concerning the circulation-dependent convective heating have been advanced and tested in terms of prototype linear models. One of the earliest hypotheses follows

Corresponding author address: Dr. Bin Wang, Department of Meteorology, University of Hawaii, 2525 Correa Road, Honolulu, HI 96822.

wave–CISK thinking (Hayashi 1970; Lindzen 1974) with an emphasis on the interaction of equatorial Kelvin waves and convective heating (Lau and Peng 1987; Chang and Lim 1988). This mechanism provides a naive explanation for a slow eastward propagation of vertically out-of-phase zonal wind anomalies along the equator. Another hypothesis, as proposed by Emanuel (1987) and Neelin et al. (1987), considers the feedback between anomalous evaporation and surface winds. Even without equatorial waves, the east–west asymmetry in the heating created by differential evaporation can induce a slow, eastward-moving Walker-type circulation cell in the presence of a uniform easterly basic flow. The last hypothesis invokes a feedback between convective heating and tropical boundary-layer dynamics (Wang 1988; Wang and Rui 1990b). The boundary-layer convergence couples the baroclinic and barotropic modes in the free troposphere in such a way that the generation of eddy available potential energy is more efficient for planetary-scale waves than for short waves.

The convective interaction with circulation is inherently nonlinear even for small amplitude disturbances. Testing the three mechanisms with a more realistic conditional (or positive only) heating scheme is necessary. With the conditional heating scheme, equatorial wave–CISK was shown to be able to produce an exponentially growing wavenumber one flow pattern that trav-

convection in producing slow instability (growth rate of an order of 10^{-6} s^{-1}), organizing multiscale convective complex, coupling moist Kelvin and Rossby waves, and forming a dispersive wave packet. The model is capable of reproducing some observed key features of TIS and sheds physical insight into the basic dynamics of tropical intraseasonal oscillation.

2. A basic theoretical framework: $2\frac{1}{2}$-layer model

a. Model physics

The model is designed to contain only the essential physics necessary for simulating fundamental features of the observed TIS. There are two types of nonlinearity that are involved in moist dynamics: advection of momentum and temperature and circulation-dependent heating. The nonlinear advection is important when the wave amplitude is finite and the period is comparable to the advective time scale. The circulation-dependent heating, on the other hand, acts even for small amplitude perturbations regardless of the wave properties. To keep the model as simple as the essential physics will allow, we will consider only conditional heating and neglect advective nonlinearity in this study.

In order to include all three feedback mechanisms mentioned in the previous section, we assume a model atmosphere consisting of a two-layer free troposphere and a well-mixed boundary layer. The model is an ex-

ity in the boundary layer and the lower tropospheric layer, which are estimated by

$$q_e = q_0(p_s^m - p_e^m)/m(p_s - p_e), \qquad (2.2a)$$

$$q_3 = q_0(p_e^m - p_2^m)/m(p_e - p_2), \qquad (2.2b)$$

where pressure p_s, p_e, and p_2 have been divided by 1000 hPa; and $m = H/H_1$ with $H = 7.6$ km being the density scale height and $H_1 = 2.2$ km being the water vapor density scale height. In the derivation of (2.2a,b) it was assumed that the absolute humidity of the basic-state atmosphere falls off with height exponentially with a constant water vapor density scale height H_1 (Wang 1988). The surface air specific humidity q_0 is assumed to be a function of SST (in units of °C) given by the following empirical formula (Li and Wang 1994):

$$q_0 = (0.972 \text{ SST} - 8.92) \times 10^{-3}. \qquad (2.3)$$

The model, which is composed of a two-level free troposphere and a well-mixed boundary layer, describes three vertical modes: baroclinic and barotropic modes of the free troposphere and a boundary-layer mode. The convective heating released in the middle troposphere stimulates only the baroclinic mode. It has been demonstrated that the variations associated with the barotropic mode are substantially smaller than the variations associated with the baroclinic mode for tropical instability (Wang and Rui 1990b) and for forced tropical motion (Wang and Li 1993). If vertically integrated divergence in the free troposphere vanishes the barotropic and baroclinic modes are decoupled even in the presence of a boundary layer. A fundamental simplification made here is to remove the barotropic mode by assuming that the column integral of divergence in the free troposphere vanishes. With this simplification the model describes only two vertical modes: the free-troposphere baroclinic mode and the boundary-layer mode. In this sense, the present model may be referred to as a 2¹/₂-layer model.

The dimensional governing equations on an equatorial β plane are

$$\partial u/\partial t - \beta y v = -\partial \phi/\partial x + r\nabla^2 u, \qquad (2.4a)$$

$$\partial v/\partial t + \beta y u = -\partial \phi/\partial y + r\nabla^2 v, \qquad (2.4b)$$

$$C_0^{-2}\partial \phi/\partial t + (1 - \delta I)\nabla \cdot \mathbf{V}$$

$$= d(\delta B - 1)\nabla \cdot \mathbf{V}_B - \delta F C_E |\mathbf{V}_B|/h, \qquad (2.4c)$$

$$\partial u_B/\partial t - \beta y v_B = -\partial \phi/\partial x - E u_B, \qquad (2.4d)$$

$$\partial v_B/\partial t + \beta y u_B = -\partial \phi/\partial y - E v_B, \qquad (2.4e)$$

where $\mathbf{V}(u, v)$ and $\mathbf{V}_B(u_B, v_B)$ are the lower-troposphere and boundary-layer winds, respectively; ϕ is the lower-troposphere geopotential perturbation; r is a horizontal momentum diffusion coefficient; C_0 denotes dry gravity wave speed of the free-troposphere baroclinic mode; $d = (p_s - p_e)/\Delta p$ is nondimensional depth of

the boundary layer; $h = \Delta p/\rho_s g$, where Δp is one-half pressure depth of the free troposphere; and $E = \rho_s g A_z/[(p_s - p_e)h_0 \ln(h_0/z_0)]$ is friction coefficient in the boundary layer, where A_z, h_0, and z_0 are given in Table 1. In the thermodynamic equation (2.4c) the remaining three nondimensional parameters are defined as follows:

$I = q_3/q_c$ heating coefficient due to

wave convergence   (2.5a)

$B = q_e/q_c$ heating coefficient due to

frictional convergence   (2.5b)

$F = (q_s - q_0)/q_c$ heating coefficient due to

evaporation,   (2.5c)

where $q_c = 2C_p p_2 C_0^2/(bR\Delta p L_c)$, and R, L_c, and C_p are gas constant for dry air, latent heat of condensation, and specific heat at constant pressure, respectively. Quantity q_c stands for a vertical mean specific humidity in the lower-tropospheric layer, which is needed to produce a vanishing effective static stability in the present model.

From the thermodynamic equation (2.4c), one can readily identify three mechanisms: wave–CISK represented by parameter I, evaporation–wind feedback denoted by parameter F, and CFC feedback represented by parameter B. Note also that the moisture contents (q_e, q_3, q_s, and q_0) are functions of SST [see Eqs. (2.2) and (2.3)]. Therefore, the heating intensity coefficients I, B, and F are directly controlled by SST.

b. Numerical scheme and parameters

The equations are solved in an equatorial beta-plane channel. Boundary conditions in the zonal direction are

TABLE 1. Parameters and their standard values used in the experiments.

p_e	Pressure at the top of the boundary layer	900 hPa
Δ_p	Half–pressure depth of the free troposphere	400 hPa
SST	Sea surface temperature	29°C
C_0	Dry gravity wave speed of the baroclinic mode	50 m s^{-1}
r	Horizontal momentum diffusion coefficient	10^6 m^2 s^{-1}
b	Precipitation efficiency coefficient	0.9
A_z	Vertical turbulent viscosity in the boundary layer	10 m^2 s^{-1}
h_0	Depth of the surface layer	40 m
z_0	Surface roughness length	0.01 m
C_E	Heat exchange coefficient	1.5×10^{-3}
I	Heating coefficient due to wave convergence	0.84
B	Heating coefficient due to frictional convergence	1.73
F	Heating coefficient due to evaporation	0.59
E	Ekman number in the boundary layer	3×10^{-5}
d	Nondimensional boundary-layer depth	0.25
h	Half-depth of the free troposphere	3.6 km

periodic, and require, on the north and south boundaries, partial derivatives normal to the boundaries vanishing. These north–south boundary conditions ensure no fluxes of mass, momentum, and heat across the boundaries.

Finite-difference schemes in both space and time are adopted; the time increment is 30 minutes. In addition to leapfrog scheme in time, Euler and Euler-backward schemes are used every 12 hours to reduce numerical noise. Spatial resolution in standard runs is 5° longitude by 2° latitude. A finer resolution of 2.5° longitude by 2° latitude was tested for the transient boundary-layer case. The solution is not sensitive to changes in resolution.

Latent heat is assumed to be released in the precipitating regions only. Other possible switch-on functions have also been tested. For instance, convection was assumed to occur in the areas of large-scale boundary-layer convergence, so that the heating switch-on function $\delta = H(-\omega_e)$. The results obtained with the two different heating switch-on functions are quite similar (figure not shown) as long as the CFC feedback mechanism is concerned.

In the present boundary-layer model, Rayleigh friction balances the sum of the pressure gradient and Coriolis forces. For low-frequency motions, the Rayleigh friction parameterizes not only frictional effect but also the nonlinear effects of nonresolved high-frequency grid-scale processes. Diagnostic studies using monthly mean surface pressure and wind data indicated that the balance of the three major boundary-layer forces requires that Rayleigh friction coefficients vary with wind direction and latitude (Li and Wang 1994; Deser 1993). The meridional friction coefficient E_y is generally 2–3 times larger than its zonal counterpart, E_x, in the equatorial region. For this reason, we adopted $E_y = 2E_x = 2E$ in the present study. Experiments with different ratios of E_y/E_x were performed. It was found, as expected, that an increase in meridional Rayleigh friction coefficient cuts down meridional wind-induced convergence, thus reducing instability. The nature of the instability is not altered, however, by a reasonable choice of the ratio.

an arbitrary positive multiplier. Exponentially growing solutions exist for such a system (Charney and Eliassen 1964; Wang and Xue 1992; Xie et al. 1993). To determine a time-mean growth rate time integration was carried out for 40 days. The growth or decay of the mode is measured by its maximum precipitation rate, which indicates the maximum generation rate of the total (available potential plus kinetic) energy of the unstable mode. The growth rate determined in this manner is consistent with those derived from kinetic or available potential energy.

Unless otherwise stated, the parameter values used in this paper are listed in Table 1.

3. Energetics and a necessary condition for CFC feedback instability

It is useful to first examine the energetics of the free troposphere. The eddy kinetic energy equation can be readily obtained from (2.1a,b):

$$\partial/\partial t\langle(u^2 + v^2)/2\rangle$$
$$= \langle\phi\nabla\cdot\mathbf{V}\rangle - r\langle(\nabla u)^2 + (\nabla v)^2\rangle, \quad (3.1)$$

where the angle brackets denote a spatial average over the entire horizontal domain. Eddy available potential energy depends on local effective static stability. In dry ($\delta = 0$) regions the effective static stability is proportional to C_0^2. Multiplying the heat equation (2.4c) by $(1 - \delta)\phi$ and integrating the resultant equation over the entire horizontal domain leads to

$$\partial/\partial t\langle(1 - \delta)\phi^2/(2C_0^2)\rangle$$
$$= -\langle(1 - \delta)\phi\nabla\cdot\mathbf{V}\rangle - d\langle(1 - \delta)\phi\nabla\cdot\mathbf{V}_B\rangle. \quad (3.2)$$

Similarly, in wet ($\delta = 1$) regions the effective static stability is in proportion to $(1 - I)C_0^2$. Multiplying (2.4c) by $\delta\phi/(1 - I)$ and integrating over the horizontal domain yields

$$\partial/\partial t\langle\delta\phi^2/[2(1 - I)C_0^2]\rangle$$
$$= -\langle\delta\phi\nabla\cdot\mathbf{V}\rangle + [d(B - 1)/(1 - I)]\langle\delta\phi\nabla\cdot\mathbf{V}_B\rangle$$
$$[E_C /[(1 - I)]\langle\delta\phi\nabla\cdot\mathbf{V}_B\rangle \quad (3.3)$$

where K and P represent, respectively, mean eddy kinetic and available potential energy; $\langle P, K \rangle$ denotes rate of conversion from eddy available potential energy to eddy kinetic energy; GP1 and GP2 are rates of eddy available potential energy generation due to convective heating associated with boundary-layer moisture convergence and surface evaporation, respectively; $D1$ and $D2$ express energy dissipation in the boundary layer and free troposphere.

In terms of the notation in (3.4), the eddy kinetic, available potential, and total energy equations can be written as

$$\partial K / \partial t = \langle P, K \rangle - D2, \quad (3.5)$$

$$\partial P / \partial t = -\langle P, K \rangle + GP1 + GP2 - D1, \quad (3.6)$$

$$\partial (K + P) / \partial t = GP1 + GP2 - D1 - D2. \quad (3.7)$$

Equation (3.7) indicates that in a stable wave–CISK regime ($I < 1$), eddy energy is generated by convective heating associated with the boundary-layer moisture convergence (GP1) and surface evaporation (GP2). Note, however, the latter is also indirectly controlled by boundary-layer convergence as implied by $\delta = H(P_r)$ or $\delta = H(-\omega_e)$. Furthermore, it can be shown that

$$O(GP1/GP2) = O(Dq_e/(q_s - q_0)LC_D), \quad (3.8)$$

where symbol $O(\ )$ means the order of magnitude of the variable quantity within the bracket, and $L = 10^6$ m is a characteristic meridional length scale determining the boundary-layer divergence (since boundary-layer divergence is primarily attributed to meridional wind component). Nondimensional number D/LC_D is $O(1)$ and q_e is roughly three times as large as $(q_s - q_0)$ over the tropical ocean. One may infer that GP1 is approximately three times larger than GP2. We note also that GP1 depends on the covariance between geopotential perturbation and boundary-layer divergence, whereas GP2 is determined by the covariance between low geopotential perturbation and surface wind speed; both differ from that of kinetic energy generation that depends on the covariance between geopotential perturbation and free troposphere divergence.

Neglecting effects of surface evaporation and free tropospheric momentum diffusion, the instability due to CFC feedback requires GP1 > $D1$, namely,

$$\langle \delta \phi \nabla \cdot \mathbf{V}_B \rangle > [(1 - I)/(B - I)] \langle \phi \nabla \cdot \mathbf{V}_B \rangle. \quad (3.9)$$

A necessary condition for the CFC feedback instability is that the fractional covariance between geopotential perturbation and boundary-layer convergence in the wet regions must exceed $(1 - I)/(B - I)$. An increase in SST favors amplification of unstable mode by lowering the value $(1 - I)/(B - I)$ (Table 2).

Although the eddy energy for the CFC feedback instability is generated through boundary-layer convergence in precipitating areas of pressure trough (or of

TABLE 2. Quantity $(1 - I)/(B - I)$ as a function of SST for $p_e = 900$ hPa.

SST (°C)	25.0	26.0	27.0	28.0	29.0	30.0
$(1 - I)/(B - I)$	0.46	0.38	0.31	0.24	0.18	0.13

positive temperature anomaly) [Eq. (3.4d)], the realization of the instability is, in general, assisted by wave convergence heating [Eq. (3.9)]. It should be pointed out, however, that the CFC feedback instability can operate without wave convergence. An example is the case in which $I = 0$ so that no wave convergence heating exists. In that case, the forcing induced by boundary-layer moisture convergence can still lead to an amplifying perturbation. Another extreme case is $I = 1$ in which no propagating equatorial waves exist. An eastward-propagating growing mode can also be produced by CFC feedback process. Since the mean flow speed is zero in the cases under consideration, no steering level exists for the unstable mode; that is, the Miles (1961) theorem does not apply to the CFC feedback instability. Bolton (1980) has shown that for a forced perturbation to grow and to travel faster than mean-flow speed at all levels, heating must be out of phase with maximum vertical velocity. The boundary-layer convergence gives such a phase shift between heating and maximum vertical motion. In section 6 a more detailed analysis will be presented to show how the frictional effect creates such a phase shift.

The differences between CFC feedback instability and wave–CISK are conspicuous in terms of energetics. First, wave–CISK requires $I > 1$ whereas CFC feedback instability occurs when $I < 1$. Second, the generations of eddy available potential energy and kinetic energy are in phase in wave–CISK, whereas they are out of phase in CFC feedback instability. The former is thus a direct thermal instability, whereas the latter is not. The key process that is responsible for these differences is the phase shift between wave-induced convergence and boundary-layer convergence. We will further elaborate the importance of this phase shift to the instability in section 6b.

4. Low-frequency instability

To identify effects of CFC feedback, we first consider a steady-state boundary layer and omit the surface evaporation term in (2.4c). Assume a uniform SST = 29°C for which the wave convergence heating coefficient I is less than unity when the top of the boundary layer is higher than 980 hPa.

Figure 1 illustrates how perturbations may grow due to increased frictional–convergence heating. For a shallow boundary layer ($p_e = 950$ hPa), an initial perturbation decays slowly with an exponential decay rate of about 0.03 day^{-1}. This is due to the fact that the destabilizing effect of the frictional convergence heat-
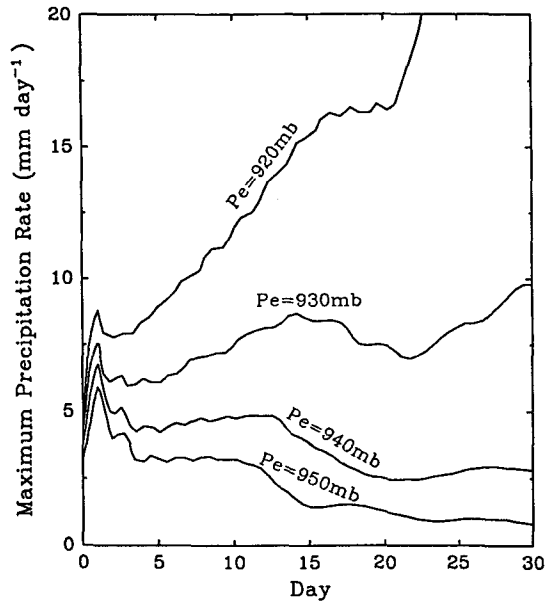
FIG. 1. Maximum precipitation rate of convection–frictional convergence feedback mode as a function of time for differing boundary-layer depths.

$O(10^{-5} \text{ s}^{-1})$ (Fig. 3). In the comparison made in Fig. 3, all model parameters are identical except in the CFC feedback case $F = 0$ (no evaporation) and $p_e = 900$ hPa, whereas in the evaporation–wind feedback case $p_e = 1000$ hPa (no boundary layer) but the evaporation term is retained. Without a boundary layer the parameter $I > 1$ when SST exceeds 28°C, implying that the unstable mode is a combined wave–CISK and EW feedback mode. Note that when SST increases the growth rate of EW feedback mode smoothly merges with that of the combined wave–CISK and EW feedback mode. In contrast, the CFC feedback generates a distinctive low-frequency unstable mode.

When both the CFC and evaporation–wind feedbacks are included, the growth rate of the unstable mode is close to that of CFC feedback mode (Fig. 3). This implies that the effect of boundary-layer moisture convergence dominates the evaporation effect, a conclusion in accord with that derived from (3.8). Figure 4 shows that the eddy energy generation due to frictional convergence heating (GP1) is much larger than that due to surface evaporation (GP2), confirming that the dominant impact of the CFC feedback on the combined CFC and EW feedback instability. It is obvious that the low-frequency nature of the CFC feedback in-

ing is insufficient to compensate boundary-layer dissipation. When the boundary-layer depth expands, on one hand, the wave–convergence heating decreases and the moist free troposphere is effectively stabilized; on the other hand, the frictional convergence heating increases more rapidly, which eventually overcomes boundary-layer dissipation and the stabilization of the free troposphere, leading to an instability. The transition from an oscillatory decay to an oscillatory growth occurs when the top of the boundary layer rises from $p_e = 940$ to $p_e = 930$ hPa. As the boundary layer further deepens ($p_e = 920$ hPa), the amplitude increases exponentially with a growth rate of 0.06 day^{-1}.

The unstable mode that is destabilized by frictional convergence heating grows or decays slowly. The growth rate increases with increasing SST and deepening boundary layer (Fig. 2). For a fixed boundary-layer depth (925 hPa, for example), a critical SST (27.5°C) is required in order for a perturbation to amplify. For a wide range of SST (from 25° to 30°C) and a boundary layer depth of 1 km, the growth rate varies from 0 to 0.2 day^{-1}, which is $O(10^{-6} \text{ s}^{-1})$, an order of magnitude smaller than the typical growth rate of synoptic-scale disturbances. This low-frequency instability appears to qualitatively cope with the observed growth rate estimated from OLR field by Wang and Rui (1990a).

In the stable wave–CISK regime, the evaporation–wind feedback can also lead to exponentially growing modes (Xie et al. 1993); however, in the absence of planetary boundary layer the evaporation–wind feedback yields a fast growth with a typical growth rate of
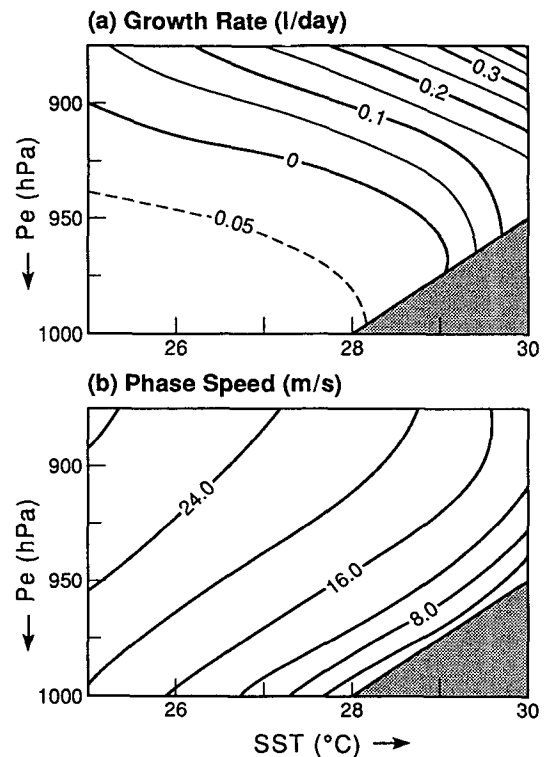

FIG. 2. (a) Growth rate and (b) phase speed of convection–frictional convergence feedback mode as functions of SST and the pressure at the top of the boundary layer. The growth rate and phase speed are averaged for the period of first 40 days. Shaded area indicates wave–CISK regime.
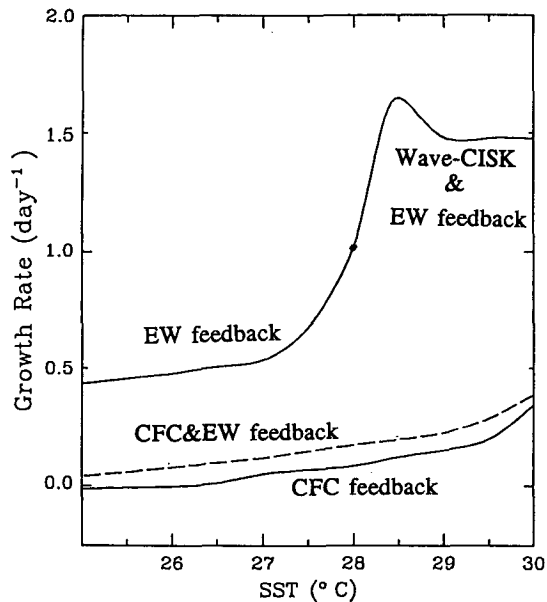
FIG. 3. Comparison of the growth rate as a function of SST between convection–frictional convergence (CFC) feedback and evaporation–wind (EW) feedback modes. The dashed curve denotes the growth rate of the combined CFC and EW feedback mode. When SST is higher than 28°C, the EW feedback mode becomes a combined wave–CISK and EW feedback mode. The growth rate is averaged for the period of the first 30 days.

stability is not altered by the presence of EW feedback mechanism. On the other hand, the presence of a boundary layer can change the fast synoptic-scale growth of EW feedback to a slow instability and eliminate its link to wave–CISK.

It should be pointed out that in the above comparison, the basic state is a resting atmosphere. The above results do not imply failure of the EW feedback mechanism, whose original model (Neelin et al. 1987; Emannual 1987) depends critically on an assumption that the mean surface wind is easterly.

The presence of a boundary layer efficiently suppresses the fast growth of the EW feedback via three means. First, the friction-induced vertical motion counteracts heating effect and offsets generation of eddy available potential energy [see the term D_1 in (3.6)]. Second, the boundary-layer friction cuts back surface wind speed, diminishing evaporational rate and generation of eddy available potential energy [see the GP2 term in (3.6)]. Last, friction changes the phase relationship between geopotential and surface wind speed in such a way that their covariance, hence the generation of the eddy available potential energy, decreases. In the equatorial precipitation region the geopotential perturbation has largest amplitude and meridional winds are small; without boundary-layer friction, the lower free troposphere zonal wind is nearly in phase with geopotential (as in an inviscid Kelvin wave), whereas in the presence of boundary-layer friction, the maximum zonal wind nearly coincides with the maximum zonal geopotential gradient. It follows that with boundary-layer friction the covariance between low geopotential and surface wind speed in the precipitating areas should be relatively small.

5. Multiscale structure and vertical tilt of divergence field

Figure 5 depicts the evolution of precipitation rate and lower-troposphere geopotential perturbation and wind fields for the CFC feedback mode with a steady boundary-layer flow. The unstable mode, after an initial adjustment, is characterized by three distinct zonal scales: a global-scale circulation system of wavenumber one; a large-scale (order of 5×10^3 km) organized multicell convective complex, and synoptic-scale (order of 10^3 km) precipitation cells. The wet core of the unstable mode occurred as a group of precipitation cells. The heating associated with the wave and boundary-layer moisture convergence integrates equatorial Kelvin and Rossby waves, forming a coupled eastward-moving Kelvin–Rossby wave packet. To the east of
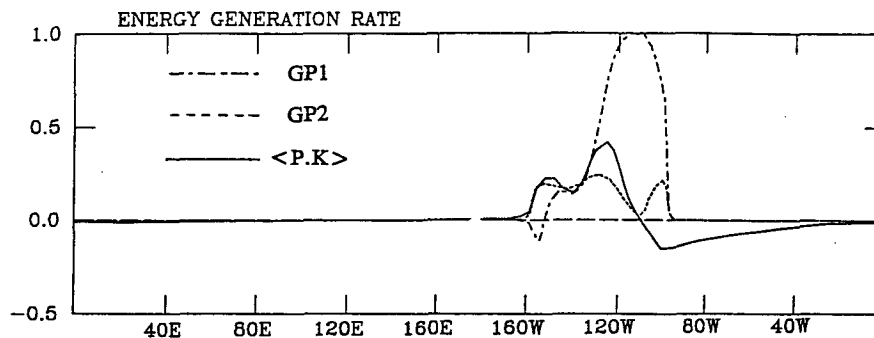

FIG. 4. The normalized rate of generation of eddy kinetic energy ($\langle P, K \rangle$) and eddy available potential energy due to frictional moisture convergence (GP1) and due to evaporation (GP2) along the equator at day 12 of the experiment with combined CFC and EW feedbacks.
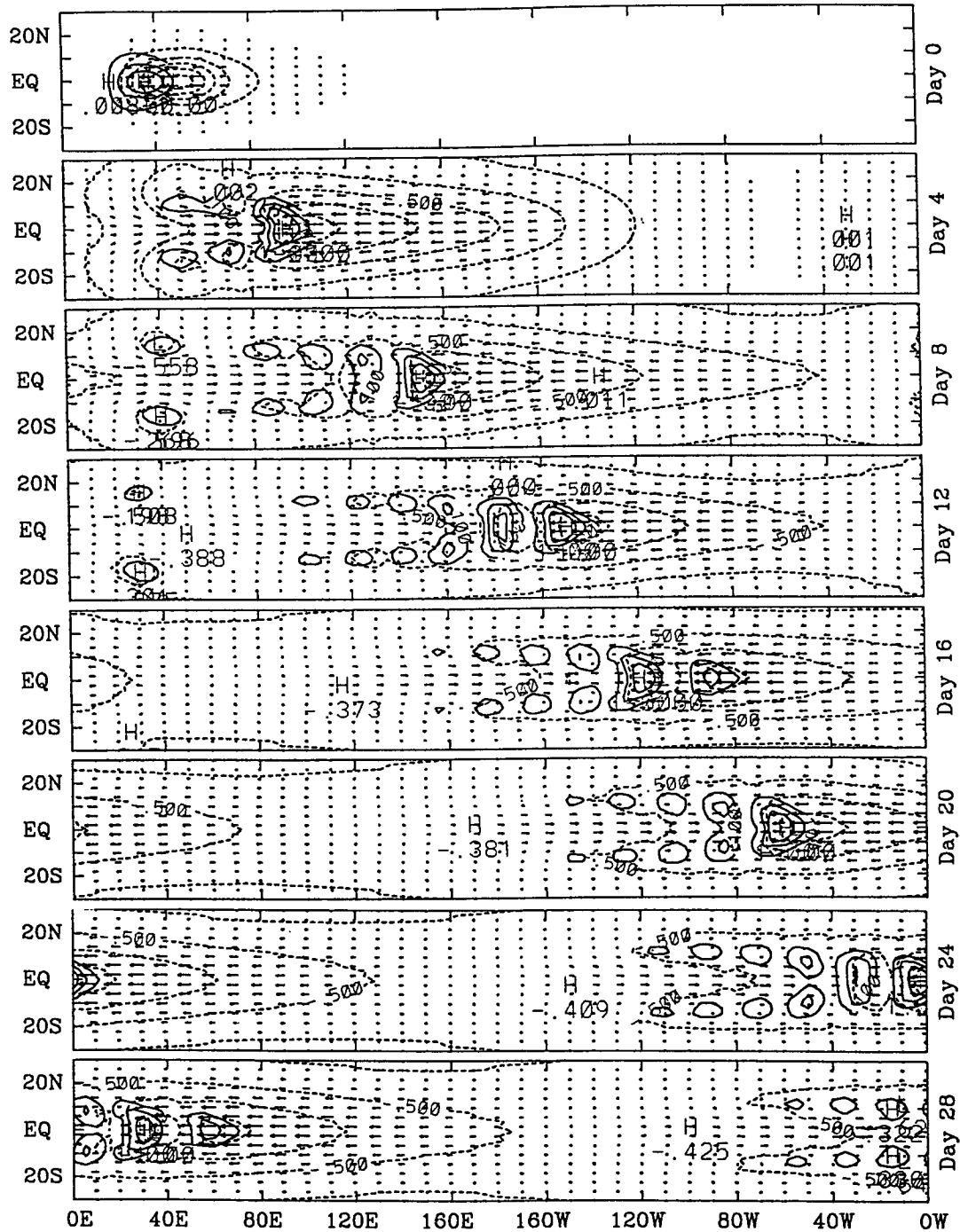
FIG. 5. Sequential maps of precipitation rate (solid-line contours) and lower troposphere geopotential perturbation (dashed-line contours) and winds (arrows) for the unstable convection–frictional convergence feedback mode in the standard experiment at interval of 4 days. All three fields are normalized by their respective maxima at each panel. The contour starts from 0.1 at an interval of 0.2.

the wave packet center strong easterlies prevail and to the west are weaker westerlies, resembling an equatorial Kelvin wave. The cyclonic shears located at each side of the equatorial westerlies maintain cyclonic vorticity cells that resemble Rossby wave trains. Along the equator convective cells coincide with Kelvin wave low pressure, and symmetric off-equatorial trains of convective cells concur with Rossby wave low pres-

sures. A similar coupled Kelvin–Rossby wave structure was found in an earlier linear analysis by Wang and Rui (1990b), but with conditional heating the unstable mode contains a much larger Rossby wave component.

The zonal wavenumber one circulation consists of a concentrated ascending (wet) region of several thousand kilometers and two much broader planetary-scale descending (dry) regions on both sides. This wet–dry asymmetry arises from the effect of conditional heating. Figure 6 illustrates how the heating creates a narrow moist core and a widespread dry zone during initial adjustment process. In the descending region dry static stability corresponds to a dry Kelvin wave speed of C_0 = 50 m s^{-1}, whereas in the precipitation region the reduced effective static stability yields a moist Kelvin wave speed of $(1 - I)^{1/2}C_0$ = 20 m s^{-1}. The narrow precipitation area was nearly in phase with zonal wind convergence $(\partial u/\partial x)$ and the minimum geopotential, and slightly lagged the maximum lower troposphere easterlies by about 10°–15° longitude. They formed a moist core and moved together eastward slowly with a moist Kelvin wave speed in the adjustment process. Outside of the precipitation region, on the other hand, the front of the easterly patch propagated at a faster dry
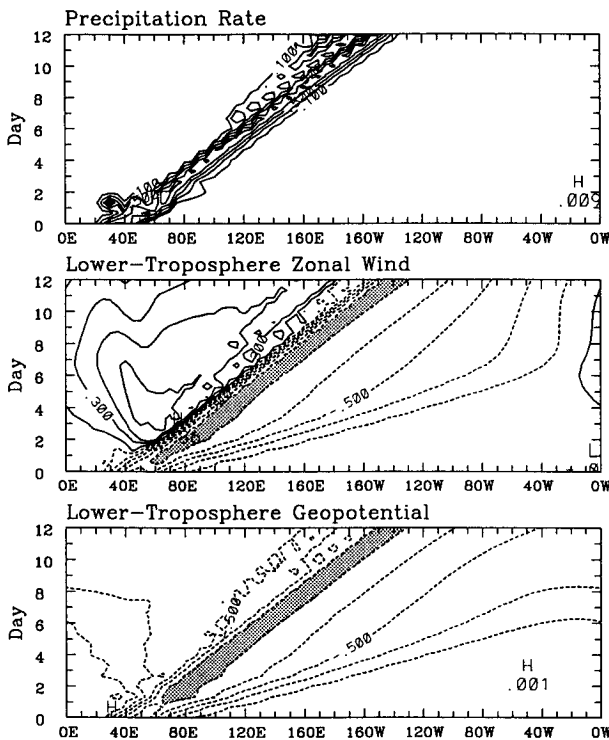

FIG. 6. Initial adjustment process in the standard experiment: Longitude–time diagram of the maximum precipitation rate and lower-troposphere geopotential and zonal wind along the equator for the unstable mode. All fields are normalized as in Fig. 5. The contour interval is 0.2. The areas enclosed by contours of 0.9 (or −0.9) are shaded to highlight the moist core region.

Kelvin wave speed and had traveled about 240° longitude in the first six days. Consequently, the low geopotential system continuously expanded until day 7. Meanwhile, the westerlies associated with Rossby wave were generated after about one day and thereafter propagated at a dry Rossby wave speed of about 17 m s^{-1} (close to one-third of the dry Kelvin wave speed), completing a westward displacement of about 70° longitude from day 2 to day 6. The expansion of the dry region was finally restrained by finite geometry of the full circumference of the globe at day 7. The formation of the wavenumber one circulation is, therefore, a result of energy dispersion by dry equatorial waves that are excited by convective heating. This process is eventually restrained by earth's finite geometry.

Boundary-layer winds, divergence, and vorticity associated with precipitation cells are shown in Fig. 7. In contrast to the global-scale free troposphere circulation, the boundary-layer winds display synoptic-scale structures that match precipitation cells extremely well. Notable equatorial westerlies accompany equatorial precipitation cells, especially the strongest westerly right beneath the most intense cell. Also notable are convergent meridional winds blowing equatorward and connecting to the strongest westerlies. The off-equatorial convective cells tend to coincide with areas of low pressure and cyclonic vorticity. Each cell tends to slightly lag boundary-layer convergence. Figure 7 reveals an intimate connection between the boundary-layer moisture flows and the organization of precipitation cells within the wave packet.

6. Effects of boundary-layer dynamics

a. Organization of convection

The relationship between boundary-layer flows and convective cells can be understood in terms of boundary-layer dynamics. For steady motion the boundary-layer vorticity (ζ) and divergence (D) equations on an equatorial β plane are, from (2.4d,e),

$$E\zeta = -\beta(v + yD), \qquad (6.1a)$$

$$ED = \beta(y\zeta - u) - \nabla^2\phi, \qquad (6.1b)$$

from which we have

$$D = -E(\nabla^2\phi + \beta u + \beta^2 yv/E)/(E^2 + \beta^2 y^2),$$
$$\quad\text{(I)}\qquad\text{(II)}\qquad\text{(III)}$$
$$(6.2a)$$

and

$$\zeta = \beta(-y\nabla^2\phi + \beta yu - vE)/(E^2 + \beta^2 y^2). \qquad (6.2b)$$

The boundary-layer convergence in the tropics comes from two principal effects: the Laplacian of geopotential [term (I) in (6.2a)] and the beta effect [terms (II) and (III) in (6.2a)]. Near the equator, the boundary-layer convergence is associated with low pressure

(a) PRECIPITATION RATE, GEOPOTENTIAL HEIGHT, BOUNDARY LAYER FLOW

(b) BOUNDARY LAYER DIVERGENCE

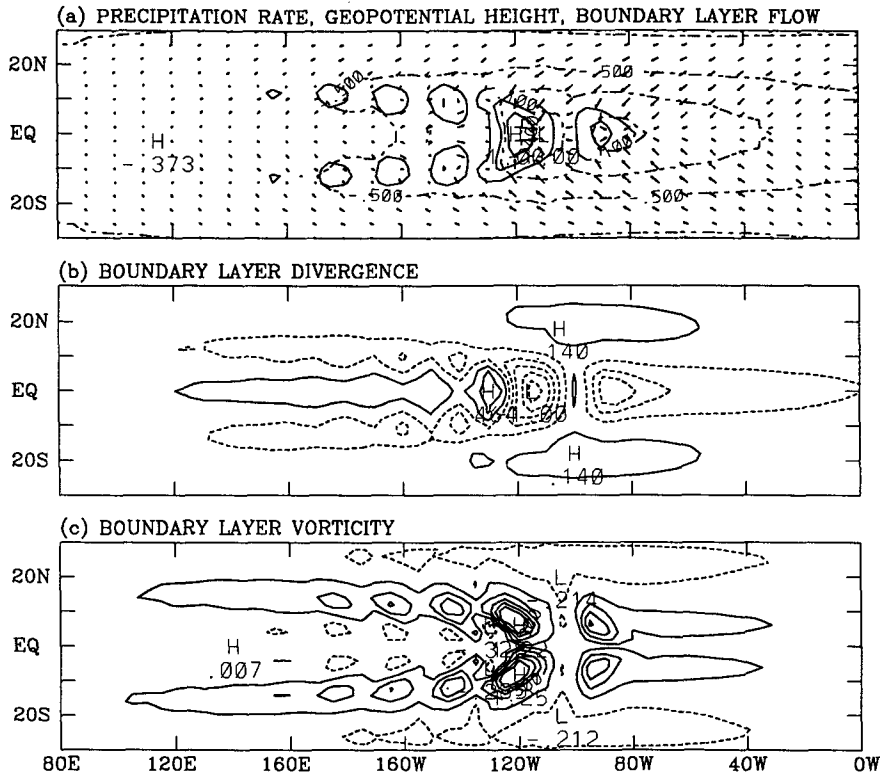## (c) BOUNDARY LAYER VORTICITY

FIG. 7. (a) Precipitation rate (solid contours) and boundary-layer winds, (b) boundary-layer divergence, and (c) boundary-layer vorticity for the standard experiment at day 16. Fields are normalized as in Fig. 5.

and westerlies [the terms (I) and (II) in (6.2a)]. For large-scale systems the latter is dominant, that is, the beta effect acting on equatorial westerlies produces an upward motion at the top of the boundary layer. This ascending motion is a mirror image of the downwelling associated with equatorial eastward oceanic currents. This explains why equatorial westerly surges are always accompanied by strong moisture convergence, which provides moist static energy source for convective heating.

Away from the equator, planetary vorticity advection [the term (III) in (6.2a)] also makes a significant contribution to boundary-layer divergence. Poleward flows cause surface convergence. This term has increasing importance to convergence as latitude increases. About one radius of deformation away from the equator, three terms in (6.2a) have comparable magnitudes. Frictional convergence, therefore, is proportional to the Laplacian of pressure and the strength of the eastward and poleward flows. This explains why precipitation cells occur on equatorward side of and within the off-equatorial pressure troughs (cyclonic vorticity areas). It is the interaction between boundary-layer moisture convergence and convective heating that maintains a coherent synoptic-scale structure of individual precipitation cells.

The vorticity at the equator is solely associated with cross-equatorial flow (6.2b): northward flow generates anticyclonic vorticity and vice versa. Notice, however, that vorticity at the equator has no contribution to boundary-layer divergence, which can be seen from the divergence equation (6.1b).

b. The phase shift between maximum upward motion and frictional convergence

Figure 8a shows that along the equator boundary-layer friction gives rise to a phase shift between the boundary-layer convergence and free troposphere wave convergence. The maximum boundary-layer convergence leads the maximum wave convergence by about 1000 km. In front of the leading convective cell the boundary-layer flows converge while the lower free tropospheric flows diverge. It was shown in section 3 that eddy kinetic energy generation, $\langle P, K \rangle$, is directly connected with wave convergence, while the eddy available potential energy generation, GP1, is identified with boundary-layer convergence. Thus, $\langle P, K \rangle$ lags GP1 by about 10° longitude (Fig. 8b).

The friction-induced phase shift marks a fundamental difference between inviscid wave–CISK and CFC feedback mechanism. In a conventional wave–CISK
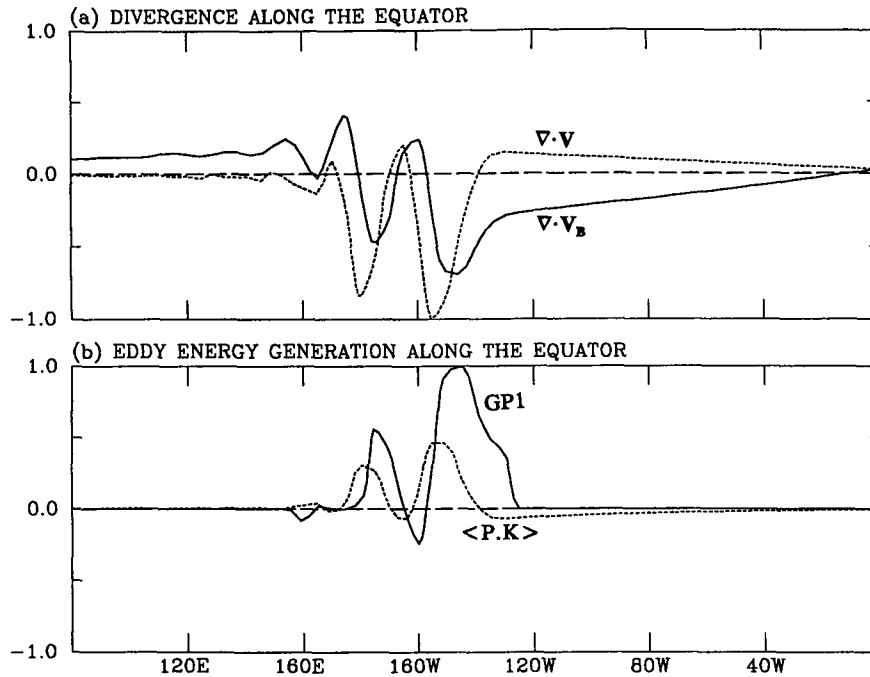
FIG. 8. (a) The lower free troposphere wave divergence ($\nabla \cdot \mathbf{V}$) and boundary-layer divergence ($\nabla \cdot \mathbf{V}_B$) along the equator, and (b) the rate of generation of eddy kinetic energy ($\langle P, K \rangle$) and eddy available potential energy due to boundary-layer convergence (GP1) along the equator at day 12 of the standard experiment. The divergence and energy generation rate were normalized by their respective maxima.
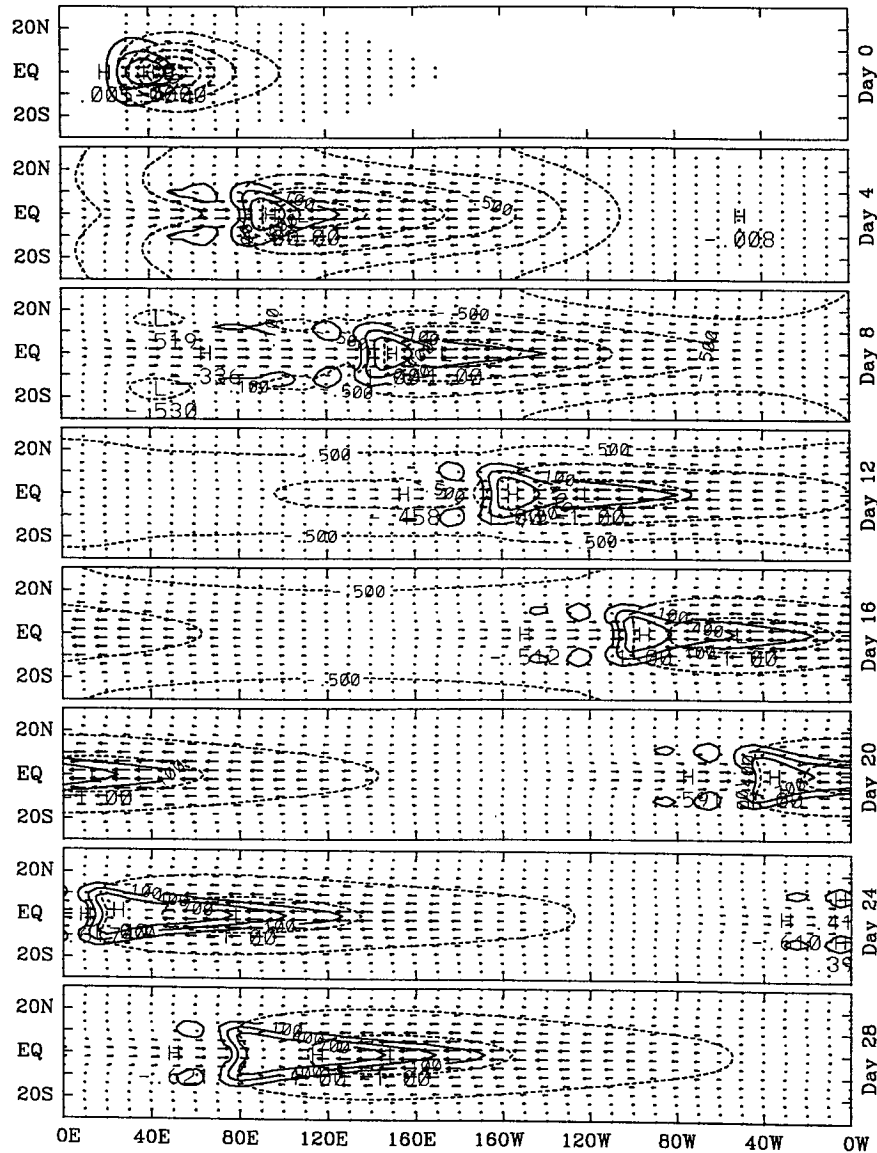
FIG. 9. As in Fig. 5 except for the case with a transient boundary-layer flow.

7. Energy propagation

Figure 5 indicates that as a leading cell moved eastward, a new cell formed behind the leading cell (at day 8), rapidly developed (at day 12), and finally became the strongest cell (at day 16) and replaced the previous leading cell (at day 20). The aforementioned process repeated itself from day 20 to day 32. We identify the propagation speed of the *maximum* precipitation rate as the group speed of the wave packet, because both the low geopotential center and the strongest easterly wind travel with the strongest precipitation cell; namely, the circulation and the convective complex move unitedly with the group speed. Individual cells within the wave

packet propagate with a faster moist Kelvin wave speed, which is $(1 - I)^{1/2}C_0$.

Figure 10 compares the group speed of the unstable wave packet with the phase speed of individual precipitation cells. The dispersion is more significant when the boundary layer becomes deep. The dispersion is also more evident when the convective heating is controlled by boundary-layer convergence, that is, $\delta = H(-\omega_e)$ (figure not shown). These results indicate an intimate link between boundary-layer convergence and energy dispersion.

When a transient boundary layer is used, the westward transfer of energy from one cell to other is not apparent, but the energy propagation speed assessed
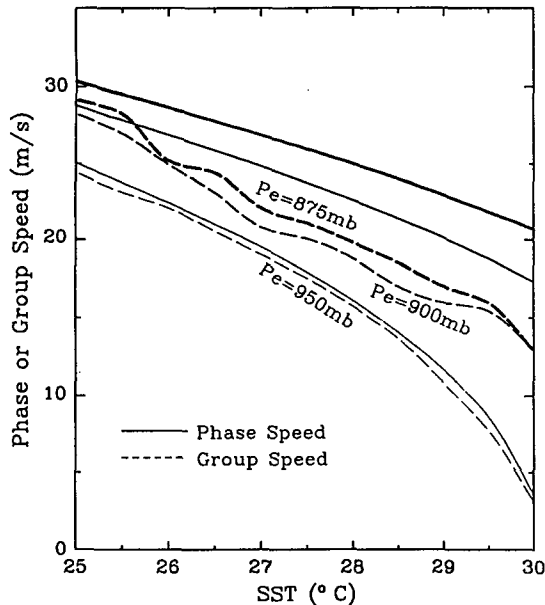
Fig. 10. Comparison of the group speed (solid line) of the convection–frictional convergence feedback mode with the phase speed (dashed line) of individual precipitation cells for differing boundary-layer depth. The thickest, medium, and thinnest lines correspond to p_e = 875, 900, and 950 hPa, respectively.

from the movement of the maximum precipitation rate is about 17 m s^{-1}, about 3 m s^{-1} slower than the moist gravity wave speed of 20 m s^{-1} (for SST $= 29°$C and $p_e = 900$ mb). This energy propagation speed is close to that of the wave packet generated by a steady boundary layer. When a linear heating scheme is adopted in the numerical experiment the wave dispersion remains visible (figure not shown). It is concluded that neither the conditional heating nor the local acceleration of the boundary-layer flow is an essential cause of dispersion.

It is the coupling between the equatorial Kelvin wave and the long Rossby wave with the gravest meridional structure via frictional convergence that creates the dispersive eastward-propagating wave packet. To demonstrate this, it suffices to consider the simplest version of the present model in which the heating is linear; evaporation is omitted; the boundary layer is steady; and the parameter $I = 1$. Equations (2.4a–e) can then be reduced to a single equation for geopotential. A linear instability problem can be readily formulated and the growth rate and frequency of the normal modes can be obtained by matrix methods or using a truncated Weber function expansion. The results show that the frequency of the unstable mode indeed varies with wavenumber. For wavenumber one with the gravest meridional structure the group speed is -1.5 m s^{-1}, meaning that the group speed is 1.5 m s^{-1} westward relative to the free atmospheric moist internal gravity waves (in this case the internal gravity wave speed is zero because $I = 1$). This is in qualitative agreement

with the results shown in Fig. 5, confirming that the dispersion is a result of the coupling between moist Kelvin and Rossby waves due to the heating produced by boundary-layer moisture convergence.

8. Conclusions and discussion

Observations have firmly established that organized cumulus convection in the tropics (e.g., cloud cluster, tropical cyclone, monsoon depression, easterly wave, intraseasonal system, and intertropical convergence zone) tend to concur with boundary-layer moisture convergence. Boundary-layer flows interacting with free tropospheric circulations and underlying SSTs, are essential for coupling convective heating with equatorial dynamics. In this paper we attempted to elucidate the roles of convective interaction with tropical boundary-layer dynamics in the dynamics of tropical intraseasonal systems (TISs).

This mechanism is an extension of the Ooyama (1964) and Charney and Eliassen (1964) CISK idea. It differs from original CISK in two aspects. First, the CISK deals with quasigeostrophic boundary-layer dynamics in an f plane, whereas the present model deals with boundary-layer dynamics in an equatorial beta plane. Section 6a elaborates this difference. Second, the CISK deals with a balanced vortex without invoking free modes of the atmosphere, whereas the present model deals with equatorial waves, the Rossby wave generated by the beta effect and Kelvin waves generated by the effects of buoyancy and the dynamic effect of the equator. Section 5 discusses the interaction between those waves and heating.

We have shown that convective interaction with tropical boundary-layer dynamics may result in unstable disturbances, which have distinctive characteristics from those of wave–CISK or evaporation–wind feedback modes in the absence of basic flows. The CFC feedback is responsible for the following features of the instability. First, it generates a low-frequency instability with a characteristic growth (or decay) rate of $O(10^{-6}$ s$^{-1})$, in contrast to a typical synoptical-scale instability of inviscid wave–CISK or evaporation–wind feedback modes. Second, the boundary-layer convergence associated with equatorial westerly surge and off-equatorial pressure trough organizes moisture supply to develop a convective complex; the heating released in the complex in turn couples equatorial Kelvin and long Rossby waves, forming a multiscale dispersive wave packet. The wave packet propagates eastward with a group speed that is smaller than the moist Kelvin wave speed. Finally, a transient boundary layer favors large-scale organization of equatorial convection and planetary-scale instability.

The intensity of TIS as measured by OLR anomalies often doubles within one to two pentads over the central equatorial Indian Ocean and the western Pacific (Wang and Rui 1990a), implying that TIS can be regarded as

a low-frequency unstable mode compared to synoptic-scale instability. The maritime continent and central Pacific are regions of decay. The slow instability and its spatial variation have not been properly addressed in the previous theoretical models. The unstable mode resulting from CFC feedback has a typical growth rate on an order of 10^{-6} s^{-1}, which increases with increasing SST for a given boundary-layer depth (Fig. 2). The preferred development over warm water of the Indian and western Pacific Oceans may be viewed as a manifestation of favorable low-frequency instability of the moist tropical atmosphere. The disintegration of convection anomalies in the eastern central Pacific results from lack of instability due to the underlying cool ocean surface. The longitudinal variation of SST thus creates a sharp contrast in the strength of intraseasonal variations between the eastern and western hemispheres (Knutson et al. 1986). The cause of the weakening over the Indonesian Archipelago, however, remains poorly understood. A plausible hypothesis is that intense diurnal variation and synoptic-scale disturbances constantly tap moist static energy, effectively reducing the energy source available for the low-frequency development. The large surface friction over the islands may be another factor causing TIS to decay.

The slow propagation of the eastward-moving TIS is a result of heating effects. The heating may slow down eastward movement through two mechanisms: reduction in static stability and generation of a dispersive wave packet through the coupling of moist equatorial Kelvin and Rossby waves. The latter results in a slow group velocity for the disturbance and represents a new mechanism revealed by the present model.

Observations have shown that convective anomalies tend to be accompanied by surface equatorial westerly surges (Nitta and Motoki 1987) and the boundary-layer convergence anomalies tend to lead convective (negative OLR) anomalies (Hendon and Salby 1994; Salby and Hendon 1994). The vertical structure of the 30–60 day mode simulated by GCM also shows the strongest upward motion in the middle troposphere lagging boundary-layer moisture convergence (e.g., Lau and Lau 1986). These observed and GCM-simulated features are difficult to reproduce in simple theoretical models. Some qualitative agreement seen in the present model can be explained by boundary-layer dynamics (section 6).

The horizontal circulation of TIS appears to be characterized by a coupling between equatorial upper-tropospheric easterlies (westerlies) with twin anticyclones (cyclones) residing on each side of the equator (Knutson and Weickmann 1987; Murakami 1988; Rui and Wang 1990). This structure was qualitatively reproduced, though in a somewhat idealized fashion.

Although the circulation anomaly of TIS exhibits a global zonal scale, the cloud (OLR) anomaly is concentrated in an area with a zonal scale of a few thousand kilometers. The wet–dry asymmetry, namely, the contrast between the global-scale circulation and the concentrated region of convective complex, is ascribed to the effect of nonlinearity associated with conditional heating. The fast-propagating dry waves outside the wet region carry energy away, maintaining a global scale of the disturbance under the restriction of the finiteness of the earth's geometry.

Within the wet region, the cloud mass exhibits a multicell structure (see, for example, Figs. 4–6 of Murakami et al. 1984; Nakazawa 1988). Although the global-scale circulation, large-scale convective complex, and synoptic-scale precipitation cells of the unstable wave packet described by Fig. 5 bear some similarity to the observed multiscale structure of the intraseasonal oscillation, the model can not simulate the westward propagating cloud cluster–scale cells. In addition, the multiscale structure is not unique to CFC feedback mechanism. Lau et al. (1989) reproduced similar multiscale structure using their five-level numerical model.

The present model has assumed a uniform SST distribution and a resting basic tropical atmosphere. It also neglected the barotropic mode in the free troposphere and the advective nonlinearity. These assumptions have effectively simplified the problem and allow us to focus on the basic dynamics of the unstable mode resulting from convection–frictional convergence feedback. The effects of basic tropical circulations and the annual variation of SST, as well as the roles of nonlinear advection of momentum and heat and the interaction between the baroclinic and barotropic mode, are currently under investigation and will be reported later.

REFERENCES

Bolton, D., 1980: Application of the Miles theorem to forced linear perturbations. *J. Atmos. Sci.*, **37**, 1639–1642.

Chang, C.-P., and H. Lim, 1988: Kelvin wave–CISK: A possible mechanism for the 30–50 day oscillation. *J. Atmos. Sci.*, **45**, 1709–1720.

Charney, J. G., and A. Eliassen, 1964: On the growth of the hurricane depression. *J. Atmos. Sci.*, **21**, 68–75.

Deser, C., 1993: Diagnosis of the surface momentum balance over the tropical Pacific Ocean. *J. Climate*, **6**, 64–74.

Dunkerton, T. J., and F. X. Crum, 1991: Scale selection and propagation of wave–CISK with conditional heating. *J. Meteor. Soc. Japan*, **69**, 449–456.

Emanuel, K. A., 1987: An air–sea interaction model of intraseasonal oscillation in the tropics. *J. Atmos. Sci.*, **44**, 2324–2340.

Hayashi, Y., 1970: A theory of large-scale equatorial waves generated by condensation heat and accelerating the zonal wind. *J. Meteor. Soc. Japan*, **48**, 140–160.

——, and D. G. Golder, 1986: Tropical intraseasonal oscillations appearing in a GFDL general circulation model and FGGE data. Part I: Phase propagation. *J. Atmos. Sci.,* **43,** 3058–3067.

——, and ——, 1988: Tropical intraseasonal oscillation appearing in a GFDL general circulation model and FGGE data. Part II: Structure. *J. Atmos. Sci.,* **45,** 3017–3033.

Hayashi, Y. Y., and A. Sumi, 1986: The 30–40 day oscillations simulated in an "aqua-planet" model. *J. Meteor. Soc. Japan,* **64,** 451–467.

Hendon, H. H., 1988: A simple model of 40–50 day oscillation. *J. Atmos. Sci.,* **45,** 569–584.

——, and M. L. Salby, 1994: The life cycle of the Madden–Julian Oscillation. *J. Atmos. Sci.,* **51,** in press.

Hsu, H.-H., B. J. Hoskins, and F.-F. Jin, 1990: The 1985–1986 intraseasonal oscillation and the role of the extratropics. *J. Atmos. Sci.,* **47,** 823–839.

Itoh, H., 1989: The mechanism for the scale selection of tropical intraseasonal oscillations. *J. Atmos. Sci.,* **46,** 1779–1798.

Knutson, T. R., and K. M. Weickmann, 1987: 30–60 day atmospheric oscillation: Composite life cycles of convection and circulation anomalies. *Mon. Wea. Rev.,* **115,** 1407–1436.

——, K. M. Weickmann, and J. E. Kutzbach, 1986: Global-scale intraseasonal oscillation of outgoing longwave radiation and 200 mb zonal wind during Northern Hemisphere summer. *Mon. Wea. Rev.,* **114,** 605–623.

Krishnamurti, T. N., P. K. Jayakumar, J. Sheng, N. Surgi, and A. Kumar, 1985: Divergent circulations on the 30–50 day time scale. *J. Atmos. Sci.,* **42,** 364–375.

Lau, K.-M., and P. H. Chan, 1985: Aspects of the 40–50 day oscillation during the northern winter as inferred from outgoing longwave radiation. *Mon. Wea. Rev.,* **113,** 1889–1909.

——, and ——, 1986: Aspects of the 40–50 day oscillation during the northern summer as inferred from outgoing longwave radiation. *Mon. Wea. Rev.,* **114,** 1354–1367.

——, and L. Peng, 1987: Origin of low frequency (intraseasonal) oscillation in the tropical atmosphere. Part I: the basic theory. *J. Atmos. Sci.,* **44,** 950–972.

——, ——, C. H. Sui, and T. Nakazawa, 1989: Dynamics of super cloud clusters, westerly wind bursts, 30–60 day oscillation, and ENSO: A unified view. *J. Meteor. Soc. Japan,* **67,** 205–219.

Lau, N.-C., and K.-M. Lau, 1986: The structure and propagation of intraseasonal oscillation appearing in a GFDL general circulation model. *J. Atmos. Sci.,* **43,** 2023–2047.

——, I. M. Held, and J. D. Neelin, 1988: The Madden–Julian oscillation in an idealized general circulation model. *J. Atmos. Sci.,* **45,** 3810–3812.

Li, T., and B. Wang, 1994: A thermodynamic equilibrium climate model for monthly mean surface winds and precipitation over the tropical Pacific. *J. Atmos. Sci.,* **51,** 1372–1385.

Lim, H., T.-K. Lim, and C.-P. Chang, 1990: Reexamination of wave–CISK theory: Existence and properties of nonlinear wave–CISK modes. *J. Atmos. Sci.,* **47,** 3078–3091.

Lindzen, R. S., 1974: Wave–CISK in the tropics. *J. Atmos. Sci.,* **31,** 156–179.

Lorenc, A. C., 1984: The evolution of planetary scale 200 mb divergent flow during the FGGE year. *Quart. J. Roy. Meteor. Soc.,* **110,** 427–441.

Madden, R. A., 1986: Seasonal variations of the 40–50 day oscillation in the tropics. *J. Atmos. Sci.,* **43,** 3138–3158.

——, and P. R. Julian, 1971: Detection of a 40–50 day oscillation in the zonal wind in the tropical Pacific. *J. Atmos. Sci.,* **28,** 702–708.

——, and ——, 1972: Description of global-scale circulation cells in the tropics with a 40–50 day period. *J. Atmos. Sci.,* **29,** 1109–1123.

Mahrt, L. J., 1972: A numerical study of the influence of advective accelerations in an idealized, low latitude, boundary layer. *J. Atmos. Sci.,* **29,** 1477–1484.

Miles, J. W., 1961: On the stability of heterogeneous shear flows. *J. Fluid Mech.,* **10,** 496–508.

Murakami, T., 1988: Intraseasonal atmospheric teleconnection patterns during the Northern Hemisphere winter. *J. Climate,* **1,** 117–131.

——, and T. Nakazawa, 1985: Tropical 45 day oscillations during the 1979 northern summer. *J. Atmos. Sci.,* **42,** 1107–1142.

——, ——, and J. He, 1984: On the 40–50 day oscillation during the 1979 Northern Hemisphere summer. Part I: Phase propagation. *J. Meteor. Soc. Japan,* **62,** 440–468.

Nakazawa, T., 1988: Tropical super clusters within intraseasonal variations over the western Pacific. *J. Meteor. Soc. Japan,* **66,** 823–839.

Neelin, J. D., I. M. Held, and H. Cook, 1987: Evaporation–wind feedback and low-frequency variability in the tropical atmosphere. *J. Atmos. Sci.,* **44,** 2341–2348.

Nitta, T., and T. Motoki, 1987: Abrupt enhancement of convective activity and low-level westerly wind burst during the onset phase of 1986–1987 El Niño. *J. Meteor. Soc. Japan,* **65,** 497–506.

Ooyama, K., 1964: A dynamic model for study of tropical cyclone development. *Geofis. Ins.* (Mexico), **4,** 187–198.

Rui, H., and B. Wang, 1990: Development characteristics and dynamic structure of tropical intraseasonal convection anomalies. *J. Atmos. Sci.,* **47,** 357–379.

Salby, M. L., and H. H. Hendon, 1994: Intraseasonal behavior of cloud temperature and motion in the tropics. *J. Atmos. Sci.,* **51,** in press.

Swinbank, R. T., T. N. Palmer, and M. K. Davey, 1988: Numerical simulation of Madden-Julian oscillation. *J. Atmos. Sci.,* **45,** 774–788.

Wang, B., 1988: Dynamics of tropical low-frequency waves: An analysis of the moist Kelvin wave. *J. Atmos. Sci.,* **45,** 2051–2065.

——, and H. Rui, 1990a: Synoptic climatology of transient tropical intraseasonal convection anomalies: 1975–1985. *Meteor. Atmos. Phys.,* **44,** 43–61.

——, and ——, 1990b: Dynamics of the coupled moist Kelvin–Rossby wave on an equatorial beta-plane. *J. Atmos. Sci.,* **47,** 397–413.

——, and Y. Xue, 1992: On the behavior of a moist Kelvin wave packet with nonlinear heating. *J. Atmos. Sci.,* **49,** 549–559.

——, and T. Li, 1993: A simple tropical atmospheric model of relevance to short-term climate variation. *J. Atmos. Sci.,* **50,** 260–284.

Weickmann, K. M., G. R. Lusky, and J. E. Kutzbach, 1985: Intraseasonal (30–60 day) fluctuations of outgoing longwave radiation and 250 mb streamfunction during northern winter. *Mon. Wea. Rev.,* **113,** 941–960.

——, and S. J. S. Khasa, 1990: The shift of convection from the Indian Ocean to the western Pacific Ocean during a 30–60 day oscillation. *Mon. Wea. Rev.,* **118,** 964–978.

Xie, S.-P., A. Kubakawa, and K. Hanawa, 1993: Evaporation–wind feedback and the organizing of tropical convection on the planetary scale. Part I: Quasi-linear instability. *J. Atmos. Sci.,* **50,** 3873–3883.